Extended Lyman-α emission towards the SPT2349-56 protocluster at $z = 4.3$

Yordanka Apostolovski, Manuel Aravena, Timo Anguita, Matthieu Béthermin, James Burgoyne, Scott Chapman, Carlos de Breuck, Anthony Gonzalez, Max Gronke, Lucia Guaita, et al.

▶ **To cite this version:**

Yordanka Apostolovski, Manuel Aravena, Timo Anguita, Matthieu Béthermin, James Burgoyne, et al.. Extended Lyman-α emission towards the SPT2349-56 protocluster at $z = 4.3$. Astronomy & Astrophysics - A&A, 2024, 683, pp.A64. 10.1051/0004-6361/202245785 . hal-03949503

HAL Id: hal-03949503
https://hal.science/hal-03949503v1

Submitted on 20 Apr 2024

HAL is a multi-disciplinary open access archive for the deposit and dissemination of scientific research documents, whether they are published or not. The documents may come from teaching and research institutions in France or abroad, or from public or private research centers.

L'archive ouverte pluridisciplinaire **HAL**, est destinée au dépôt et à la diffusion de documents scientifiques de niveau recherche, publiés ou non, émanant des établissements d'enseignement et de recherche français ou étrangers, des laboratoires publics ou privés.

Distributed under a Creative Commons Attribution 4.0 International License

A&A, 683, A64 (2024)
https://doi.org/10.1051/0004-6361/202245785
© The Authors 2024

Astronomy & Astrophysics

Extended Lyman-α emission towards the SPT2349-56 protocluster at $z = 4.3$

Yordanka Apostolovski[1], Manuel Aravena[2], Timo Anguita[3,4], Matthieu Bethermin[5], James Burgoyne[6], Scott Chapman[7], Carlos De Breuck[8], Anthony Gonzalez[9], Max Gronke[10], Lucia Guaita[3], Yashar Hezaveh[11,12], Ryley Hill[7], Sreevani Jarugula[13], Evelyn Johnston[2], Matt Malkan[14], Desika Narayanan[9], Cassie Reuter[13], Manuel Solimano[2], Justin Spilker[15], Nikolaus Sulzenauer[16], Joaquin Vieira[13], David Vizgan[13], and Axel Weiß[16]

[1] Instituto de Física y Astronomía, Universidad de Valparaíso, Avda. Gran Bretaña 1111, Valparaíso, Chile
e-mail: yordanka.apostolovski@gmail.com
[2] Instituto de Estudios Astrofísicos, Facultad de Ingeniería y Ciencias, Universidad Diego Portales, Av. Ejército 441, Santiago, Chile
[3] Instituto de Astrofisica, Facultad de Ciencias Exactas, Universidad Andres Bello, Fernandez Concha 700, Santiago, Chile
[4] Millennium Institute of Astrophysics, Monseñor Nuncio Sotero Sanz 100, Oficina 104, Santiago, Chile
[5] Aix-Marseille Univ., CNRS, LAM, Laboratoire d'Astrophysique de Marseille, 13388 Marseille, France
[6] Department of Physics and Astronomy, University of British Columbia, Vancouver, BC, Canada
[7] Department of Physics and Atmospheric Science, Dalhousie University, Halifax, NS B3H 4R2, Canada
[8] European Southern Observatory, Karl Schwarzschild Straße 2, 85748 Garching bei München, Germany
[9] Department of Astronomy, University of Florida, 211 Bryant Space Sciences Center, Gainesville, FL 32611, USA
[10] Max Planck Institut fur Astrophysik, Karl-Schwarzschild-Straße 1, 85748 Garching bei München, Germany
[11] Département de Physique, Université de Montréal, Montreal, Quebec H3T 1J4, Canada
[12] Center for Computational Astrophysics, Flatiron Institute, 162 Fifth Avenue, New York, NY 10010, USA
[13] Department of Astronomy, University of Illinois at Urbana-Champaign, 1002 West Green St., Urbana, IL 61801, USA
[14] Department of Physics and Astronomy, University of California, Los Angeles, CA 90095-1547, USA
[15] Department of Physics and Astronomy and George P. and Cynthia Woods Mitchell Institute for Fundamental Physics and Astronomy, Texas A&M University, 4242 TAMU, College Station, TX 77843-4242, USA
[16] Max-Planck-Institut für Radioastronomie, Auf dem Hügel 69, 53121 Bonn, Germany

Received 23 December 2022 / Accepted 30 November 2023

ABSTRACT

Context. Deep spectroscopic surveys with the Atacama Large Millimeter/submillimeter Array (ALMA) have revealed that some of the brightest infrared sources in the sky correspond to concentrations of submillimeter galaxies (SMGs) at high redshift. Among these, the SPT2349-56 protocluster system is amongst the most extreme examples given its high source density and integrated star formation rate.

Aims. We conducted a deep Lyman-α line emission survey around SPT2349-56 using the Multi-Unit Spectroscopic Explorer (MUSE) at the Very Large Telescope (VLT) in order to characterize this uniquely dense environment.

Methods. Taking advantage of the deep three-dimensional nature of this survey, we performed a sensitive search for Lyman-α emitters (LAEs) toward the core and northern extension of the protocluster, which correspond to the brightest infrared regions in this field. Using a smoothed narrowband image extracted from the MUSE datacube around the protocluster redshift, we searched for possible extended structures.

Results. We identify only three LAEs at $z = 4.3$ in this field. This number is lower than expectations for blank fields, and is significantly lower than the number of previously identified SMGs in this system. We find an extended Lyman-α structure of about 60×60 kpc^2 in size located 56 kpc east of the protocluster core. Three SMGs coincide spatially with the location of this structure. All the other SMGs are undetected in Lyman-α emission, which is consistent with the conspicuous dust obscuration in these systems. We conclude that either the three co-spatial SMGs or the protocluster core itself are feeding ionizing photons to the Lyman-α structure.

Key words. galaxies: formation – intergalactic medium

1. Introduction

Studies of massive galaxies at the peak of their star-formation activity and their relation to the densest protocluster systems are key to understanding the hierarchical formation of the most massive galaxy structures in the early Universe. Current studies seek to understand the role of feedback from active galactic nuclei (AGN; Pike et al. 2014; Smolčić et al. 2017), or the relation between downsizing and star formation during the active growth phases of such structures (Magliocchetti et al. 2013; Miller et al. 2015).

Cosmological simulations show that cold dark matter (CDM) haloes merge and form a web-like network traced by young galaxies and reionized gas. A protocluster will form at the highest overdensity regions within this filamentary structure at early cosmic times ($z \sim 4$–6; Baugh et al. 1998; De Lucia & Blaizot 2007), eventually becoming a massive virialized cluster by $z < 1$ (e.g., Overzier 2016). These cosmological simulations indicate

Open Access article, published by EDP Sciences, under the terms of the Creative Commons Attribution License (https://creativecommons.org/licenses/by/4.0), which permits unrestricted use, distribution, and reproduction in any medium, provided the original work is properly cited.
This article is published in open access under the Subscribe to Open model. Subscribe to A&A to support open access publication.

that galaxies within galaxy protoclusters experience a luminous starburst phase. The denser protoclusters are the sites of violent interactions and massive star-formation, and AGN activity, where high radiation fields, galactic winds, and outflows are triggered (e.g., Overzier 2016).

To identify and study these starbursting protocluster systems, several observational methods or astrophysical tracers have been used. Low-frequency radio observations have typically been used to search for radio-loud quasars as tracers of massive protocluster fields (e.g., Miley & De Breuck 2008; Galametz et al. 2013; Rigby et al. 2014). Star-forming galaxies selected through their significant UV rest-frame Lyman-α emission line ($\lambda_{\rm rest}$ = 1215.67 Å), which are referred to as Lyman-α emitters (LAEs), appear to be ubiquitous in these fields, showing 3–5 times larger overdensity factors than the field at the same redshift (Pentericci et al. 1997; Kurk et al. 2000; Venemans et al. 2002, 2004, 2005, 2007; Croft et al. 2005).

Narrowband image surveys in protocluster fields have identified a population of LAEs with luminosities of greater than $10^{43.4}$ erg s^{-1} and large spatial extensions (40−150 kpc). These structures are often referred to as Lyman-α blobs (LABs; Steidel et al. 2000; Matsuda et al. 2004). The origin of the emission of these structures can be explained by different scenarios, such as the presence of AGN or massive star-forming galaxies. The production of Lyman-α photons in these objects could be associated with different processes, such as recombination radiation, continuum pumping, or collisional excitation (see; Cantalupo 2017).

Indeed, the use of the Lyman-α emission line as a tracer of cold gas in large-scale structures has recently gained significant interest, yielding the identification of several massive protocluster systems associated with giant (or enormous) Lyman-α nebulae (LANs) at high redshift. Examples of this include the discovery of an extreme overdensity of four luminous AGN and quasars embedded in a giant LAN and a LAE overdensity SDSSJ0841+3921 at z = 2.0 (Hennawi et al. 2015), a massive overdensity linked to the luminous, enormous LAN BOSS1441 at $z \sim 2.32$ (Cai et al. 2016, 2017); the overdensity of CO emitters around the MAMMOTH-1 nebula at z = 2.32, associated to the BOSS1441 structure (Li et al. 2021); and the massive Lyman-α structure SSA22 at z = 2.3 (Umehata et al. 2019).

An alternative way is to search for groups of submillimeter galaxies (SMGs; also known as dusty star-forming galaxies, or DSFGs) as tracers of massive structures at high redshift. Given the relatively low number density of SMGs in the sky (e.g., ∼100 deg^{-2} at $S_{850\,\mu\rm m} > 5$ mJy Karim et al. 2013), searching for overdensities of SMGs in wide-area submillimeter surveys offers a unique method to pinpoint obscured star-formation activity in young protocluster systems (e.g., Chapman et al. 2009; Daddi et al. 2009; Aravena et al. 2010; Capak et al. 2011; Casey et al. 2015; Miller et al. 2018; Oteo et al. 2018; Hill et al. 2020; Wang et al. 2021). Given the negative K-correction at these wavelengths, observations in this regime enable us to search for the most distant structures out to z = 7. Particular examples of rare massive protocluster systems revealed through this technique are the Distant Red Core (DRC) at z = 4.0 (Oteo et al. 2018) and the SPT2349-56 system (Miller et al. 2018), which is the subject of this paper (see below). The DRC system was found to harbour ten SMGs within a small area (∼260 × 300 kpc^2), which was confirmed through submillimeter spectroscopy of CO and [C I] lines, and to have a collective star formation rate (SFR) of 14 000 $M_\odot$ yr^{-1}. Most relevant for this work is the detection of extended Lyman-α emission close to the core center, yet no Lyman-α emitters in the 1 arcmin^2 covered by MUSE observations (Oteo et al. 2018).

The large-scale millimeter survey covering 2500 square degrees of the sky conducted with the South Pole Telescope (SPT; Carlstrom et al. 2011) discovered a population of millimeter-bright sources ($S_{1.4\,\rm mm} > 20$ mJy; Vieira et al. 2010, 2013; Everett et al. 2020; Reuter et al. 2020). Follow-up observations with the Atacama Large Millimeter/submillimeter Array (ALMA) showed that the majority of these sources are gravitationally lensed SMGs (>90%) with magnifications of $\mu_{870\,\mu\rm m} \sim$ 5−20 (median $\mu_{870\,\mu\rm m}$ = 6.3 Hezaveh et al. 2013; Spilker et al. 2016). The remaining sources show no evidence of gravitational lensing, being either intrinsically bright or composed of fainter multiple-component SMGs or groups of SMGs (Wang et al. 2021). The high number of SMGs spread over a small area of the sky (<1′) found in these fields strongly suggests the existence of (sub)millimeter-bright protocluster fields (Wang et al. 2021).

Among the sample of SPT protoclusters, the SPT2349-56 system stands out due to its exceptionally high surface density of SMGs. SPT2349-56 is located at z = 4.304 and has a surface density of more than ten times the average blank-field value and a volume density of 1000 times the average (Miller et al. 2018; Hill et al. 2020). This system could represent the core of a massive galaxy cluster and is one of the most massive structures known to date in the early Universe. The SPT2349-56 system has two main infrared(IR)-bright structures as seen in the Atacama Pathfinder EXperiment (APEX) Large Bolometer Camera (LABOCA) 870 µm maps, following the north–south direction (Fig. 1). The southern component alone displays a flux density of $S_{870} \approx 77$ mJy, whereas the northern component contributes $S_{870} \approx 33$ mJy. For reference, a typical unlensed SMG has a flux density of around 5–10 mJy at 870 µm. Higher-resolution deep ALMA spectroscopy yielded a total of 24 [CII] and 16 CO(4–3) line emitters in the southern and northern extensions of the cluster (e.g., Miller et al. 2018; Hill et al. 2020). Several components of this system have SFR estimates of ∼1000 $M_\odot$ yr^{-1}, while the full protocluster system is estimated to have a SFR of about 6.6×10^4 $M_\odot$ yr^{-1} (Hill et al. 2020). Similarly, the dynamical mass of the core region is estimated to be $\sim 9 \times 10^{12}$ $M_\odot$, while the total halo mass of the whole structure is $\sim 2.5 \times 10^{13}$ $M_\odot$ (Hill et al. 2020).

The physical properties of these sources indicate that this protocluster already harbors massive galaxies that are rapidly forming stars from an abundant gas supply. The large number of SMGs in this system pushes and challenges theoretical models seeking to explain the origin and evolution of protoclusters (Chiang et al. 2013). Due to the proximity of the SMG members in the core of the protocluster (the diameter is about 130 kpc), it is likely that its component galaxies will merge to form a massive elliptical galaxy at the core of a lower-redshift Coma-like galaxy cluster (Miller et al. 2018; Hill et al. 2020). A recent search for Lyman break galaxies (LBGs) in the extended SPT2349-56 environment found four LBGs in the southern part of the protocluster (Rotermund et al. 2021), indicating that most of the SMGs are inconspicuous at optical wavelengths, with only one of the four LBGs coinciding with a previously reported SMG.

Motivated by the significant overdensities found in protocluster fields, we conducted an independent census of star-forming galaxies in the SPT2349-56 field through a sensitive search for Lyman-α emission using deep optical spectroscopy obtained with the Multi-Object Spectroscopy Unit (MUSE) at the Very Large Telescope (VLT). In Sect. 2, we describe the observations and reduction of the MUSE data towards SPT2349-56, and summarize previous observations. In Sect. 3, we present

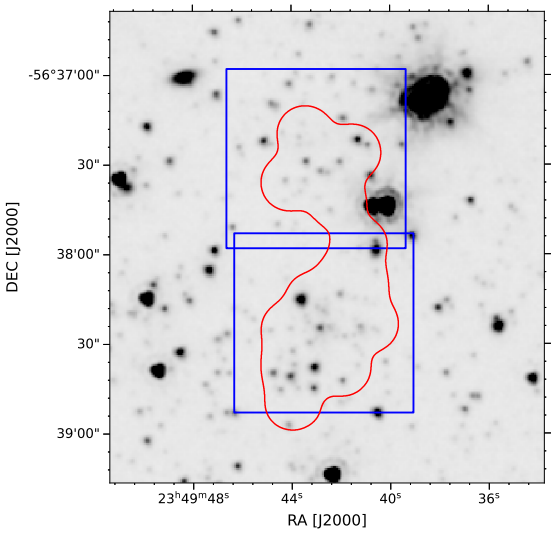

Fig. 1. Deep IRAC mosaic obtained toward the SPT2349-56 system. Red contours show the ALMA [CII] coverage. Blue squares show the observed MUSE footprint, where we used two pointings to cover the full IR-bright region previously detected with LABOCA.

the detection of Lyman-α emission through both a blind search and narrowband imaging. In Sect. 4, we analyze the nature of the extended Lyman-α emission along with its connection with LAEs and the structure of the protocluster. In Sect. 5, we present a summary of our conclusions from this work. Hereafter, we adopt a flat ΛCDM cosmology with $h = 0.677$, $\Omega_m = 0.307$, and $\Omega_\Lambda = 0.693$ (Planck Collaboration XIII 2016).

2. Observations

In this section, we describe details of the Lyman-α line observations in the SPT2349-56 protocluster at $z = 4.3$.

2.1. MUSE observations

Observations with MUSE at the VLT UT4 were performed in two separate pointings targeting the north and south extensions of the SPT2349-56 protocluster system (Fig. 1). MUSE covers the wavelength range 480–930 nm. Each pointing covers roughly 1 square arcmin (60″ × 60″). These observations were carried out in the wide field mode (WFM) in service-mode observing as a part of projects 0100.A-0437(A) and 0100.A-0437(B) (PI: M. Aravena) during dark time. Each pointing was observed for 5 h (a total of 10 hours) between November 2017 and September 2018. Each pointing consisted of a set of exposures of 680 s each, with individual exposures rotated by 90 degrees with respect to each other.

The average seeing of these observations was 0.97 and 0.98 arcsec for the southern and northern pointings, respectively, after correction of air mass. Weather conditions were classified by ESO as clear (CL; 55%), with high wind (CL-WI; 11%) and photometric conditions (PH; 33%) for all observing blocks (OBs).

We reduced the data using the MUSE pipeline v2.6 (Weilbacher et al. 2014) for bias subtraction, flat-fielding, and wavelength and flux calibration, resulting in a single data cube for each of the five OBs per field. We combined the five OB data cubes per field using the MUSE Python Data Analysis Framework (MPDAF; Bacon et al. 2016). The data cubes were merged using a sigma-clipped mean with $\sigma_{\rm clip} = 5$. As the field is relatively sparse (especially in Lyman-α at $z = 4.304$), we used Zurich Atmosphere Purge (ZAP; Soto et al. 2016) to perform a sky subtraction using principal component analysis (PCA). For this process, we used a mask in order to avoid spaxels that contained obvious continuum sources and performed sky subtraction for each individual exposure prior to combination. We used a "median" value for the ZAP parameter zero-level correction and continuum filter type, and a continuum filter size of 300.

Finally, we used the Line Source Detection and Cataloging Tool (`LSDCat`; Herenz & Wisotzki 2017) to create a median-filtered continuum-subtracted cube, which was then used to search for line emission (see below). This yielded an rms level (1σ) of 15×10^{-20} erg s^{-1} cm^{-2} Å^{-1} in the continuum-subtracted cube in a region without sources and a velocity range of ± 1500 km s^{-1} (between 6420 and 6480 Å). This corresponds to a surface-brightness limit (5σ) for line emission for a typical 300 km s^{-1} line width of 1.9×10^{-19} erg s^{-1} cm^{-2} arcsec^{-2} and a luminosity limit (5σ) for a point source of $L_{\rm lim} = 10^{41.24}$ erg s^{-1}.

2.2. Previous ALMA observations

In this study, we used the images, cubes, and locations of protocluster members previously identified through ALMA Cycle 5 and 6 observations for reference. These observations and the corresponding data reduction and source identification are described in detail by Miller et al. (2018) and Hill et al. (2020) and we refer the reader to those papers for full details.

Briefly, observations of the redshifted [CII]$_{158\,\mu\rm m}$ fine structure line towards the SPT2349-56 system were obtained using ALMA in Band 7. These were centered at a frequency of $\nu_{\rm obs} = 358.4$ GHz, yielding an average synthesized beam size of 0.43″ × 0.34″ and 3σ sensitivities of $\approx$0.3 mJy beam^{-1}. These observations, which cover the full IR-bright region, led to the identification of 24 [CII] emitters in the field. The MUSE observations described above fully cover the region observed by ALMA in Band 7 with uniform sensitivity (Fig. 1). Based on the identified [CII] sources, the mean redshift of the system was determined to be at $z = 4.304$ (Miller et al. 2018; Hill et al. 2020).

2.3. HST imaging

We used HST/Wide Field Camera 3 (WFC3)-IR images under program 15701 (PI: S. Chapman). The target was assigned two orbits for the $F110W$ filter and three orbits for the $F160W$ filter in the IR channels. Dithering was implemented for maximum resolution. The data were reduced using the standard HST pipeline. The pixel size in the WFC3 images is 0.075″. The final rms reached in these images is 0.50 nJy for the $F110W$ filter (corresponding to a 5σ AB magnitude limit of 30.4), and 0.79 nJy for the $F160W$ filter (corresponding to a 5σ AB magnitude limit of 29.9).

3. Results

We used the MUSE observations obtained toward SPT2349-56 to perform a systematic search for Lyman-α emission with three methods: a blind automatic search in the cube, creating a narrowband image around the known protocluster redshift, and a search for Lyman-α emission in (dusty) sources that had previously been identified in this field. Below, we describe each of these searches.

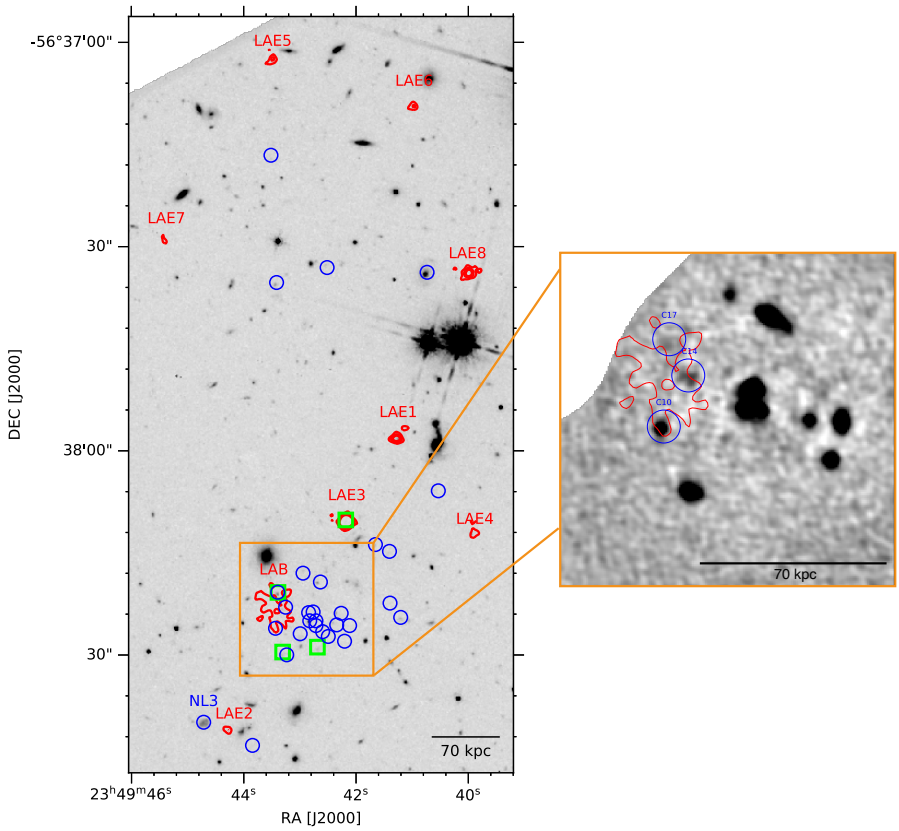

Fig. 2. Lyman-α emission toward the SPT2349-56 protocluster system at $z = 4.3$. *Left:* the area covered by MUSE is shown, with the HST $F160W$ image in the background in gray scale, and red contours representing a rendered Lyman-α image. The latter was obtained as the average of each individual line map of the detected LAEs and the LAB, in steps of 2, 5, and 7σ, where σ is the rms noise level in the average image. The blue circles highlight the locations of the ALMA [CII] and CO(4–3) line detections in the field (Miller et al. 2018; Hill et al. 2020). Green squares show the locations of the LBGs in the field (Rotermund et al. 2021). *Right:* map of ALMA [CII] line emission toward the identified Lyman-α blob (LAB) shown in the background, with blue circles representing the location of the previously identified [CII] line emitters C10, C14, and C17 (see Table 2; Hill et al. 2020). Red contours show the Lyman-α emission of the LAB at 2, 5, and 7σ.

3.1. Blind search

We performed a blind search for Lyman-α emission in the MUSE data cubes using `LSDCat` and the continuum-subtracted version of the cube. We focused on a 4000 km s^{-1} band centered on the redshifted ($z = 4.304$) Lyman-α wavelength ($\lambda_{\rm red} = 6444.2$ Å). The `LSDCat` routine detects emission lines through a spatial and spectral filtering (3D matched-filtering) approach and sorts them into discrete objects. This method is used to maximize the signal-to-noise ratio (S/N) of the entire cube, thus creating a S/N detection cube. To determine an appropriate threshold for detection in the S/N cube, we also conducted an unbiased line search in the negative version of our original cube (multiplied by -1). Assuming that the noise in this reduced velocity range of the cube is symmetric around zero and roughly follows a Gaussian distribution, the detections obtained in the negative cube will set the maximum level at which we expect line features produced by noise. From this, we find that the most significant feature in the negative cube is found at $(S/N)_{\rm det} \sim 5$, which we take as our detection threshold.

This process yields a significant number of positive features located at the edges of the independent channel images, and with line widths of one or two channels only, which we remove from our catalog as they are unphysically narrow. To filter the Lyman-α line candidates from spurious positive features, we constrain the full width at half maximum (FWHM) of the detected lines to the range of widths found for the [CII] and CO(4–3) lines for sources in the field (Hill et al. 2020), which correspond to 50−600 km s^{-1}. After this selection process, we identified eight LAE candidates: four in the northern and four in the southern pointing (Fig. 2).

We extracted the spectra of each of the LAE candidates using apertures with radii of 1 arcsec. Due to the more extended spatial nature compared to the other LAEs, we extracted the spectra of sources LAE3 and LAE8 using apertures of 2 arcsec radius (Fig. 3). Based on the significance of each of the line candidates measured in these apertures (see Fig. 3 and Table 1), we split the sample into secured LAEs and tentative candidate sources.

Only three sources are securely detected in this fashion (LAE1, LAE3, and LAE8), and the remaining five sources are therefore considered tentative detections. All the spectra were manually inspected and searched for other lines that would point to a lower redshift possibility. However, all line detections were consistent with Lyman-α at $z \sim 4.3$.

LAE1 is associated with detections in all available broadband images, including g, r, and i through the K_S band (see Appendix B in Hill et al. 2022). However, if the galaxy is at $z \sim 4.3$, we would expect it to be faint in the g band due to the Lyman break. Inspection of the HST $F110W$ image (see Fig. C.1) suggests that the excess g-band emission comes from a foreground object along the line of sight. Indeed, due to the mismatch between MUSE Lyman-α position and the optical broadband position, Hill et al. (2022) lists its photometry as upper limits (see their Table 1). The significance of the detected line and the lack of other line features in the MUSE spectrum strongly favor the $z \sim 4.3$ spectroscopic confirmation. As a precedent, we note that ALMA source C1 (source "A") appears to be well detected in g-band, because there is a foreground $z = 2.5$ galaxy as shown in Rotermund et al. (2021).

LAE3 and LAE8 are both undetected in the g-band and have faint detections in the deep r and HST $F110W$ images (see Fig. C.1 and Appendix B in Hill et al. 2022); they are significantly detected in Lyman-α without other line identifications, and have considerable EWs compared to the other sources identified in this field. Based on the redshift implied by the identified Lyman-α lines, we computed a median velocity offset

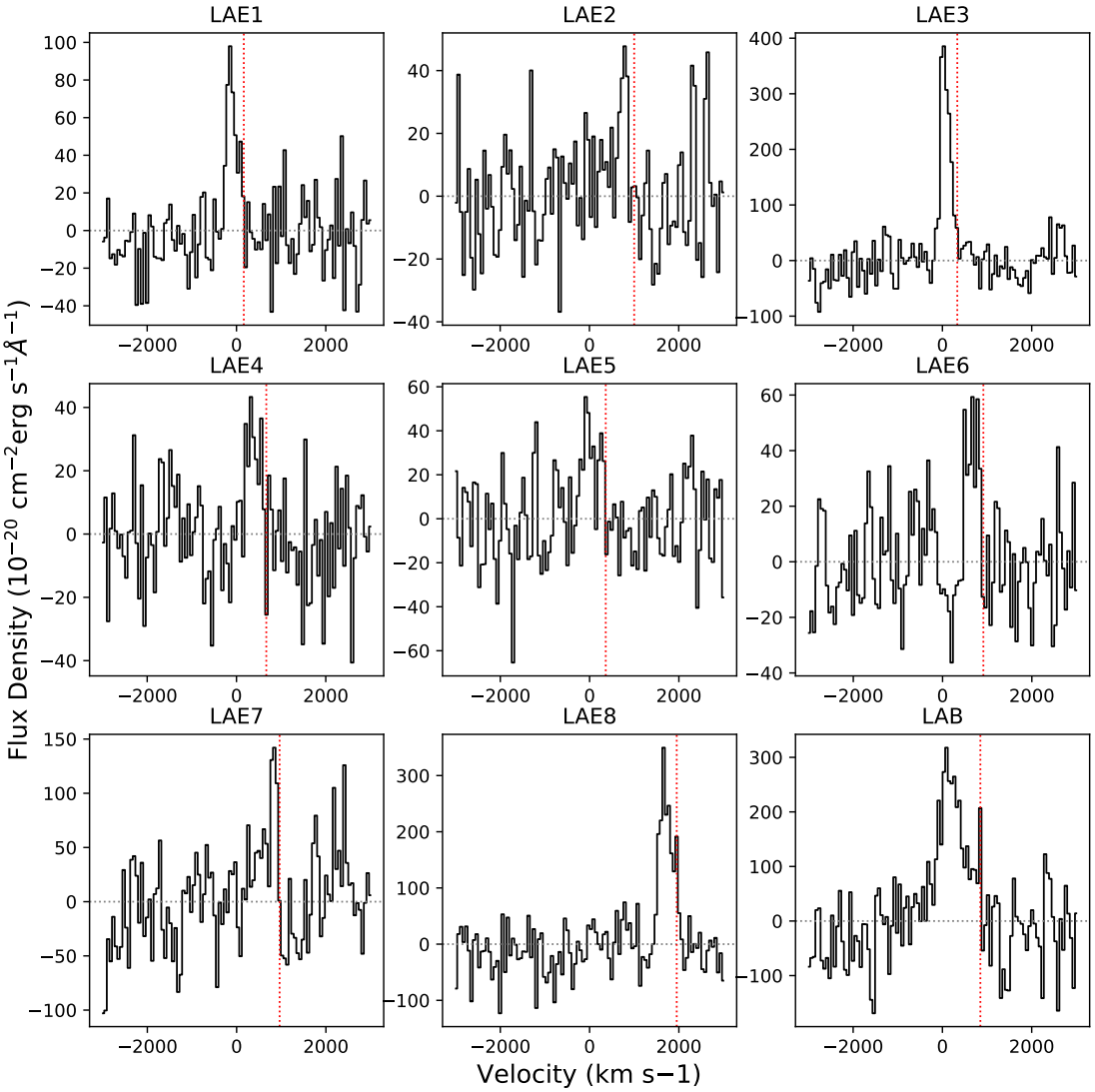

Fig. 3. Continuum-subtracted spectra of the Lyman-α emission line identified significantly within the MUSE footprint around SPT2359-56. The spectra are centered at the central velocity of the protocluster (λ = 6444.2 Å). The measured fluxes are given in Table 1. The red dotted line shows the redshift determined using the prescription from Verhamme et al. (2018). The nomenclature of the LAEs does not follow the signal-to-noise ratio of the emission lines.

for all LAEs in the field with respect to the protocluster redshift $z = 4.304$ (obtained from previous [CII] and CO identifications; Miller et al. 2018; Hill et al. 2020). As the redshift derived from the Lyman-α emission can be offset from the systemic redshift of the galaxy, we performed a statistical correction to the systemic redshift of each galaxy using the relation described in Verhamme et al. (2018). The northern and southern LAEs are found to have average velocity offsets of $\Delta v = 520$ and $\Delta v = -785$ km s^{-1}, respectively.

3.2. Narrowband image

To independently search for line emission in the field, we produced a continuum-subtracted narrowband image using a spectrally and spatially smoothed version of the MUSE datacube. The motivation for performing both spectral and spatial smoothing is to increase the sensitivity to faint, low-surface-brightness emission, specifically for finding extended structures. We selected a central wavelength for the image of the Lyman-α line redshifted to $z = 4.304$ and a width of 2000 km s^{-1} (i.e. 6401.3−6487.2 Å). We performed all these steps using the tasks provided by the LSDCat software. First, we subtract an in-spectral-direction median-filtered version of the datacube from the original datacube. We run this task with the default settings of LSDCat, with a full width of the running median of 180 Å. The spectral smoothing was therefore applied using a filter FWHM of 300 km s^{-1}, and the spatial smoothing was performed using the subtracted median filtered datacube. The narrowband image obtained is shown as a zoomed version in Fig. 2, and in its full extent in Appendix A. This image has an rms of 1.3×10^{-20} erg cm^{-2} s^{-1}.

As a result, we found an extended Lyman-α structure toward the east of the protocluster core, which we associate with a so-called "Lyman-α blob" (LAB, see Fig. 2). This extended structure is the only source found at >6σ (peak pixel) in the narrowband image aside from the previously identified LAEs and continuum sources in this field. The Lyman-α emission of the LAB subtends a roughly circular region with an area of 10″ × 10.4″ in the sky (≈70 × 70), and is located about 56 kpc east of the center of SPT2349-56. With a radius of ≈5″ (34.4 kpc), this yields

an area of $\pi r^2 = 3720\,\mathrm{kpc}^2$ or $\sim 60 \times 60\,\mathrm{kpc}^2$. We note that the LSDCat search, which was specifically performed to find point sources, found eight independent (point) sources in this region, but only through the smoother version of the narrow-band image did it become clear that these belonged to the same structure.

To obtain a spectrum of this extended emission, we draw a polygon around this source, containing all pixels detected above 2σ in the narrowband image (see Figs. 2 and 3). Here, σ corresponds to the rms value in the narrowband image obtained above $1.3 \times 10^{-20}\,\mathrm{erg\,cm^{-2}\,s^{-1}}$ (see Appendix A). Based on the Lyman-α profile, we find that the extended feature shows a line with a FWHM of about $760\,\mathrm{km\,s^{-1}}$ and a velocity offset with respect to the [CII]/CO protocluster redshift of $\Delta v = 365\,\mathrm{km\,s^{-1}}$. As the Lyman-$\alpha$ line is skewed, we measured the velocity offset by directly comparing the redshift implied by the peak of the Lyman-α profile with that of the protocluster. To compute the FWHM, we simply measured the velocities at which the intensity falls to half the maximum intensity in the Lyman-α profile. We note that the velocity offsets and FWHM derived are consistent with those obtained using a single Gaussian fit. After integrating along the full width of the line emission, we obtain a flux of $S_{\mathrm{Ly}\alpha} = 3663 \times 10^{-20}\,\mathrm{erg\,cm^{-2}\,s^{-1}}$.

A comparison of the position of the LAB with the location of the previously identified SMGs in this field (Miller et al. 2018; Hill et al. 2020) shows that three sources overlap spatially with the western part of the blob. These sources, called C10, C14, and C17 using the nomenclature of Hill et al. (2020), were identified based on their bright [CII] line emission, with fluxes of 2.96, 1.70, and $0.93\,\mathrm{Jy\,km\,s^{-1}}$, respectively. These galaxies are not the most luminous in the sample of [CII] emitters in the SPT2349-56 system, and are located at about 65 kpc from the center of the protocluster.

3.3. Previously known protocluster members

In addition to the independent searches described above, we searched the MUSE datacubes for Lyman-α emission at the positions of the previously identified SMGs in the SPT2349-56 system at $z = 4.3$. All of these sources have confirmed systemic redshifts based on the identification of the [CII] and CO(4–3) lines with ALMA (Hill et al. 2020).

For each of these sources, we extracted a spectrum using apertures with radii of 2″ centered at the location of either the [CII] or CO(4–3) detections (Fig. B.1). Inside the range of $6000\,\mathrm{km\,s^{-1}}$ centered at $z = 4.304$, we do not find significant Lyman-α emission in any of the previously confirmed SMGs in the field. The individual spectra for each source are shown in Appendix B. As shown in the previous section, source C14 is embedded in the LAB. However, the Lyman-α emission measured at its position within the 2″ aperture is weak and thus cannot be considered a detection. The LAB appears only when integrating the emission over larger scales.

Furthermore, we find a tentative detection of Lyman-α emission from one of the ALMA continuum sources for which no redshift confirmation was possible using the [CII] or CO(4–3) lines, source NL3. This source shows possible Lyman-α emission at a velocity of $-1600\,\mathrm{km\,s^{-1}}$ from the cluster core redshift ($z = 4.304$). This velocity is covered by the ALMA CO observations but not by the [CII] ones. Thus, while the ALMA [CII] observations missed the line, it is possible that either the source is too faint in CO(4–3) emission or the tentative Lyman-α feature is not real. We therefore tag this as a tentative candidate here.

We note that stacking of the MUSE spectra to yield a constraint on the average Lyman-α emission in these undetected SMGs is difficult. Several studies have demonstrated that the Lyman-α emission line does not always trace the systemic redshifts of the galaxies due to IGM scattering and absorption (e.g., Shapley et al. 2003; Song et al. 2014; Hashimoto et al. 2015). Therefore, aligning the MUSE spectra at the [CII]- or CO-derived systemic redshifts or correcting them to the rest-frame will yield a diluted Lyman-α stack signal. While corrections for the Lyman-α-derived to the systemic redshifts (or velocities) as a function of equivalent width have been calibrated, these are statistical in nature and will not yield the precise redshifts or velocities necessary for stacking. We do use such corrections in our check to see if the identified LAEs are gravitationally bound to the protocluster core (see the following section).

Finally, there are several similarities between the Lyman-α emission identified in this protocluster and that found in the DRC protocluster at $z = 4.0$ by Oteo et al. (2018). Notably, in both cases, there is evidence for a LAB close to the center of the protocluster structure. In the DRC structure, the identified LAB extends over a region of $\sim$60 kpc, similar to the extent of the LAB identified in SPT2349-56. Although Oteo et al. (2018) do not report the flux for the Lyman-α emission for the LAB, these authors find that the Lyman-α line is significantly wide, with a full width at zero intensity (FWZI) of greater than $2000\,\mathrm{km\,s^{-1}}$, whereas in the SPT2349-56 LAB the FWZI is $\sim 1500\,\mathrm{km\,s^{-1}}$. This difference is related to the possibly different nature of each system, particularly dust obscuration and geometry, which leads to differences in the direction of escaping photons. In these two cases, the LAE sizes are smaller than other LABs found in the literature for protocluster systems at high redshift, whose sizes typically range between 100 and 400 kpc (e.g., Chiang et al. 2015; Swinbank et al. 2015; Geach et al. 2016; Cai et al. 2017).

It is interesting to note that these latter authors do not find any Lyman-α emitter within their 1′ MUSE footprint. In our case, we find eight LAEs (excluding the LAB), although none of them are linked to the central part of the overdensity, which is where all the SMGs reside, but not the LAB. Similar results are found in other dense SMG protoclusters, in which LAE or Hα line-emitting galaxies trace different sources from the SMGs (e.g., Arrigoni Battaia et al. 2018; Zhang et al. 2022).

4. Analysis and discussion

4.1. Lyman-α emitters

As we show in the results section, we find eight blindly selected LAEs and one LAB. Three of the blind identifications are considered secure, and five are tentative based on their low significance (see Table 1). As shown in Fig. 2, the LAB and four of the identified LAEs are located in the southern structure, while the rest are located in the north. The locations of the LAEs and candidates range from 95 to 580 kpc from the core of the protocluster, and the implied velocities for Lyman-α appear redshifted with respect to its systemic redshift.

The significant mass of the central core of the protocluster is $\sim 9 \times 10^{12}\,M_\odot$, making it possible that most of the galaxies identified in the core neighborhood are gravitationally bound, as already shown by Hill et al. (2020). To test whether the identified Lyman-α emitters are also bound, which may yield insights into the future evolution of the LAEs within the SPT2349-56 system, we compared the offset velocities of each of the protocluster members as a function of distance from the protocluster core (Fig. 4). For the ALMA-identified protocluster members, we show their [CII]/CO-based velocities, while for the LAEs, we show their Lyman-α-based velocities. For the latter, we obtained

Table 1. Results of the blind line, narrowband, and prior selected sample search in the MUSE data cubes.

ID ...	RA (J2000)	Dec (J2000)	Δv [‡] (km s^{-1})	$FWHM$ (km s^{-1})	$S_{\mathrm{Ly}\alpha}$ (10^{-20} erg cm^{-2} s^{-1})	EW (km s^{-1})
LAB	23:49:43.39	−56:38:23.49	−450 ± 108	760 ± 40	3660 ± 1030	1530
LAE1	23:49:41.28	−56:37:58.20	−362 ± −68	330 ± 20	510 ± 150	540
LAE3	23:49:42.18	−56:38:10.48	−193 ± 79	330 ± 50	2220 ± 280	1230
LAE8	23:49:40.03	−56:37:34.11	1426 ± 71	330 ± 30	2300 ± 430	1300
Tentative candidates [†]						
NL3	23:49:44.73	−56:38:39.99	−1818 ± 39	270 ± 90	210 ± 150	1705
LAE2	23:49:44.26	−56:38:40.90	476 ± 69	330 ± 50	190 ± 170	570
LAE4	23:49:39.90	−56:38:12.22	52 ± 65	380 ± 30	240 ± 170	830
LAE5	23:49:43.47	−56:37:02.37	−362 ± 78	440 ± 50	370 ± 240	670
LAE6	23:49:40.96	−56:37:09.18	424 ± 67	310 ± 50	330 ± 200	560
LAE7	23:49:45.41	−56:37:28.70	455 ± 70	320 ± 30	320 ± 220	1170

Notes. [†]List of Lyman-α line candidates, which showed $(S/N)_{\mathrm{det}} > 5$ as computed in the LSDCat detection cube. Despite the high S/N obtained in the "maximal" LSDCat extraction, these detections are considered tentative based on their low significance measured in the original cube through homogeneous 1″ radial aperture measurements. [‡]Velocity offset relative to the protocluster's mean [CII]-derived redshift of $z = 4.304$ and corrected following Verhamme et al. (2018).

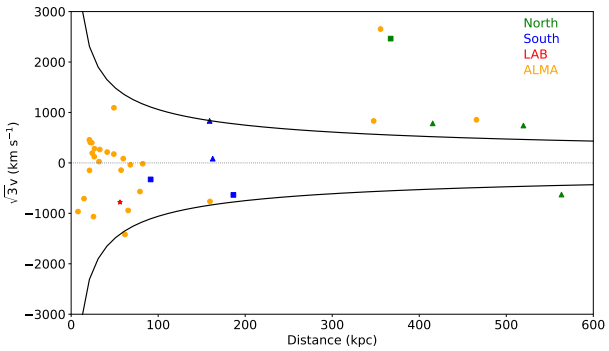

Fig. 4. Velocity offset scaled by $\sqrt{3}$ – as an estimate for 3D velocity – centered at the center of the protocluster (Hill et al. 2020) versus projected distance from the 850 μm-weighted center of the protocluster. Orange circles show detections of [CII] and CO(4–3) with ALMA (Miller et al. 2018; Hill et al. 2020), green square and triangles show Lyman-α emitters detected and candidates, respectively, in the extended emission showed by LABOCA observations (Fig. 1), blue squares and triangles show the Lyman-α emitters detected and candidates, respectively, in the southern pointing, and the red star shows the Lyman-α blob inside the 90 kpc defined as the effective radius. Black lines show the escape velocity from the protocluster. The measured velocity offset uncertainties are negligible, and therefore error bars are smaller than the size of the symbols.

a statistical correction to the systemic redshift of each galaxy using the relation described in Verhamme et al. (2018). Galaxies that have velocities lower than the escape velocity envelope at a given radius from the protocluster core are expected to be bound to the structure. The southern LAEs appear to be consistently associated with the protocluster core, including the LAB. Only one of the identified LAEs in the southern structure (a tentative candidate) resides outside the escape velocity $v_{\mathrm{esc}} = \sqrt{2GM/R}$ envelope. Conversely, most of the northern LAEs, including the secure LAE8 identification, appear to be unbound and redshifted with respect to the protocluster core, yet they follow the trend of the other [CII] identified sources. The fact that the northern LAEs follow the velocity offset of the ALMA [CII] sources in the north bolsters the interpretation of the northern structure as an unbound or infalling subhalo (e.g., Miller et al. 2018; Hill et al. 2020). In addition, this supports the idea that the southern structure, which includes the protocluster core, is likely already reaching a virialized form.

We compared the number of LAEs found in the SPT2349-56 field at $z = 4.3$ with the expected number of LAEs in the field using the ultradeep MUSE observations in the *Hubble* Ultra Deep Field (HUDF mosaic area of 3×3 arcmin^2; Inami et al. 2017). We used the Lyman-α luminosity function derived for galaxies at $z = 4-5$ in the HUDF (using Table 1 of Drake et al. 2017) and integrated down to the Lyman-α luminosity reached by our observations of $\log(L_{\mathrm{Ly}\alpha}) = 41.25$, restricting the covered area and volume to that covered by our Lyman-α search ($z = 4.25-4.36$). This yields an expected number of ≈18 LAEs in the field within the area of 2 arcmin^2 covered by our observations of SPT2349-56. Considering the detection of four secure LAEs (including the LAB) or nine potential sources in total, this implies an underdensity of LAEs in the SPT2349-56 system with respect to the field, and strengthens the case that most of the emission output and mass in this system is associated with heavily dust-obscured sources.

A possibly more extreme case in this sense is that of the IR-bright DRC protocluster system at $z = 4.0$, where no LAEs were found within 1′ of the system's center (Oteo et al. 2018). In this scenario, where almost all rest-frame UV emission is highly obscured, the existence of widespread Lyman-α emission close to the center of the protocluster systems, as seen in SPT2349-56 and DRC, is surprising, and could be enabled in a scenario where the Lyman-α emission escapes in a preferential, less obscured direction.

4.2. Insights into the nature of the extended Lyman-α emission

As mentioned above, the extended Lyman-α emission found in the MUSE-based narrowband image broadly coincides with the position of three SMGs that were identified as part of the protocluster structure. This suggests a possible physical relationship between them, as indicated by previous studies of LABs at high redshift (e.g., Chapman et al. 2001; Umehata et al. 2015; Geach et al. 2016; Oteo et al. 2018).

Cen & Zheng (2013) constructed a model for the origin of extended Lyman-α emission in the context of the cold dark

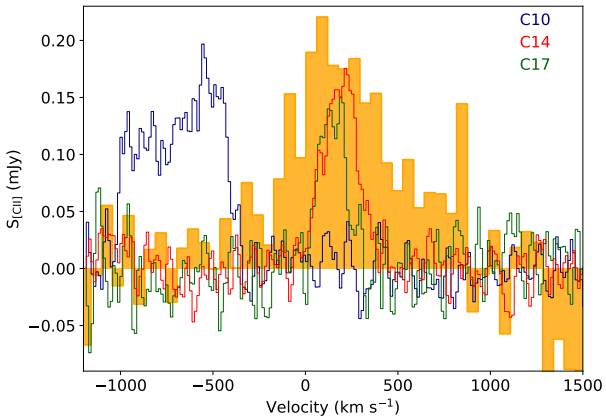

Fig. 5. Observed [CII] line profiles obtained with ALMA for sources C10, C14, and C17 (see, Hill et al. 2020), which overlap spatially with the Lyman-α Blob obtained with MUSE (see Fig. 2). The scaled Lyman-α profile is shown in orange for reference. The velocity scale refers to $z = 4.304$ for all emission lines. The Lyman-α spectra is not corrected by Verhamme et al. (2018).

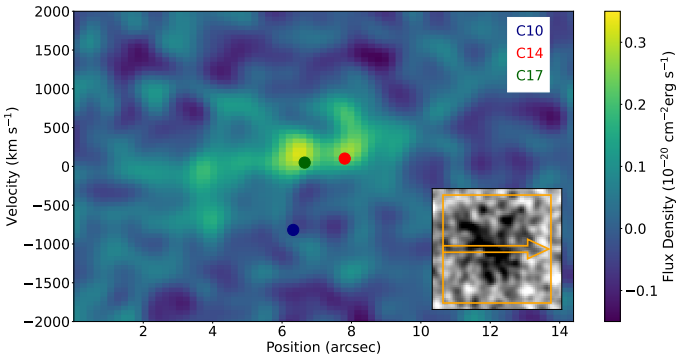

Fig. 6. Position–velocity diagram towards the Lyman-α blob extracted from MUSE cube at 0 degrees of inclination toward the east. Blue, red, and green circles show the observed [CII] emissions (C10, C14, and C17) from Hill et al. (2020). The inset shows the slit used to extract the position–velocity map across LAB using the narrowband image (Sect. 3.2). The Lyman-α velocity is not corrected by Verhamme et al. (2018). This shows a spatial connection between the LAB and two SMG members of the PC.

matter framework, in which the LAB are produced due to starburst activity. The model incorporates AGN feedback, although this latter is expected to make a subdominant contribution (e.g., Webb et al. 2009). For extended Lyman-α emission in a protocluster, each galaxy member contributes to the whole Lyman-α emission, yielding a variety of sizes and geometries typically found within a contiguous structure. The relative contribution of these SMGs depends on the dust attenuation of Lyman-α photons and the propagation and diffusion process through the circumgalactic medium (CGM) and intergalactic medium (IGM) of each member.

In Fig. 5, we compare the Lyman-α spectra of the LAB with the [CII] emission line spectra of the three SMGs spatially coincident with it: C10, C14, and C17. The [CII] line emission is expected to trace the kinematics of each host galaxy and to therefore probe the galaxies' systemic velocities and geometries (rotation, merger, etc). Due to obscuration and absorption by the IGM, the Lyman-α spectrum is expected to be redshifted with respect to the galaxies' systemic velocities and thus with respect to the [CII] lines. In this case, the Lyman-α spectrum of the LAB is found $\sim$300 km s^{-1} redward of the protocluster core velocity ($v = 0$ km s^{-1}) and $\sim$100 km s^{-1} redward of the C14 and C17 SMGs. A much larger velocity difference is seen between the LAB and the systemic velocity of the C10 galaxy. The inconsistency in velocities for C10 suggests this source might be unrelated to the Lyman-α emission. We explore this issue in more detail in the following sections.

4.3. The protocluster core as the possible origin of the LAB

The LAB is located $\sim$56 kpc to the east of the protocluster core, and is therefore within the protocluster effective radius defined by Hill et al. (2020). Along with the velocity connection between the LAB and the SMGs, this spatial coincidence suggests a physical link between the protocluster core and the LAB. It is therefore possible that the powering source of the extended Lyman-α emission is star formation or AGN activity in the starbursting SMGs at the protocluster center, where the Lyman-α photons are produced in a photon-ionized medium.

In this scenario, it is possible that most of the Lyman-α photons along our line of sight are not absorbed and/or scattered but are instead able to escape toward the eastern part of the protocluster core. Indeed, Vernet et al. (2017) observed similar regions with offsets of $\sim$100 kpc in the haloes of high-redshift AGN-host galaxies, invoking similar arguments.

Following Furlanetto et al. (2005), the Lyman-α emission can be used to yield an estimate of the underlying SFR from the powering source. For star formation episodes following a Salpeter initial mass function (Salpeter 1959) and where two-thirds of the ionizing photons are absorbed in the dense ISM, we have:

$$L_{\mathrm{Ly}\alpha} = 10^{42}(\mathrm{SFR}/[M_\odot\ \mathrm{yr}^{-1}])\ \mathrm{erg\ s}^{-1}. \quad (1)$$

Taking the value of $L_{\mathrm{Ly}\alpha} = 1.32 \pm 0.37 \times 10^{42}$ erg s^{-1}, we obtain a SFR for the extended emission of $1.32 \pm 0.37\ M_\odot$ yr^{-1}, which is orders of magnitude lower than the SFR estimates for any of the SMGs in the field. This is consistent with the idea that most (99%) of the UV radiation is obscured by dust within the SMGs.

Recent radio imaging of the SPT2349-56 field using the Australia Telescope Compact Array (ATCA) and the Australian Square Kilometer Array Pathfinder (ASKAP) found strong radio emission from the protocluster core complex (Chapman et al. 2024). The steep radio spectrum found clearly indicates that at least one of the three central sources (B, C, and G in the nomenclature used by Miller et al. 2018, or C3, C6, and C13 following Hill et al. 2020) hosts a radio AGN. This finding supports the idea that enhanced Lyman-α emission at the LAB location is produced by AGN activity at the protocluster core (e.g., Vito et al. 2020).

Figure 6 shows a position-velocity (PV) diagram of the Lyman-α emission of the LAB, extracted along the x-axis (0 degrees of inclination) toward the west of the MUSE datacube, with a slit width of 14.2 arcsec. Here, we note a widespread emission along the central velocity with an extension of 5 arcsec. At the edges, for the more distant structure, the emission goes towards bluer velocities. On the other hand, in the edge closer to the cluster, we have a structure that shifts to positive velocities. Another important issue is the behavior of the luminosity in the PV diagram. We can divide the structure into two different blobs, with the western being brighter than the eastern. This result is in agreement with the spectral line of the LAB, where we observe that the reddest emission is stronger and wider than the bluest emission (Fig. 5).

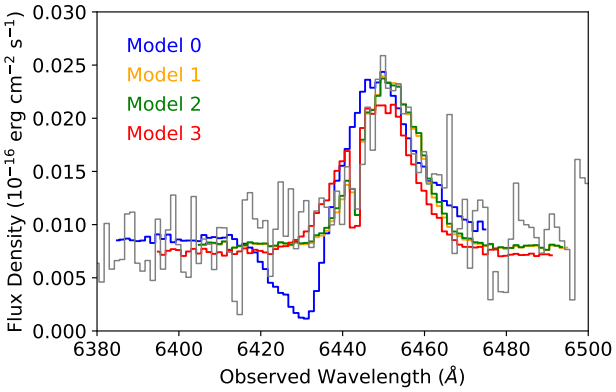

Fig. 7. Lyman-α spectrum of the LAB compared to the best-fit models that assume different systemic redshifts for the emitting source. The models are described in the text and their best-fit parameters are listed in Table 2. The best description of the observed Lyman-α spectrum is given by models 1–3, suggesting that the emission is produced by photoionization either from SMGs C14 or C17, or from the protocluster core.

4.4. Modeling the Lyman-α spectrum of the extended emission

To further explore the origin of the LAB, we test the idea that either the protocluster core or the galaxies spatially coincident with the LAB are the source of the Lyman-α emission.

We use the Lyman-α Monte Carlo Radiate Transfer code `tlac` (Gronke & Dijkstra 2014; Gronke et al. 2015) to model the Lyman-α line profile of the LAB. We utilize an expanding shell model under the assumption that one of the spatially coincident SMGs or the protocluster core is producing the LAB. Even though the geometry of the protocluster is admittedly complex and difficult to represent through the expanding shell geometry assumption, such models have been widely used in several studies to successfully reproduce the Lyman-α profiles of galaxies in different redshifts and environments (Solimano et al. 2022; Claeyssens et al. 2022). Hence, they represent a useful exercise to provide evidence for or against the proposed Lyman-α emission origin scenarios.

Our model assumes a homogeneous spherical shell that expands radially outwards, with uniformly mixed neutral gas (HI) and dust (Verhamme et al. 2006), and with the emitting source located at the center of the shell. The shell model is defined by a set of seven parameters, namely the expanding velocity ($v_{\rm exp}$), the HI column density ($N_{\rm HI}$), the dust optical depth ($\tau_{\rm d}$), the effective temperature of the gas (T), the systemic redshift of the emitter ($z_{\rm sys}$), the intrinsic equivalent width of the Lyman-α line (EW(Lyman-α)), and the intrinsic FWHM of the Lyman-α line (FWHM(Lyman-α)). For more details on these parameters, we refer the reader to Gronke et al. (2015). Given a constraint for the systemic redshift of the source and the input Lyman-α spectrum, the code yields the most likely set of parameters that reproduce the observed spectrum under the assumed geometry.

As we are interested in learning which of the underlying starburst galaxies might be producing the Lyman-α emission, we constrain $z_{\rm sys}$ using the [CII]-based redshifts of each of the possible sources of the Lyman-α line: C10 (model 0), C14 (model 1), and C17 galaxies (model 2), and the protocluster core (model 3). Instead of simply fixing $z_{\rm sys}$, we allow for a range in redshift given by the 3σ uncertainty around the measured [CII] redshift in each case. As these ranges overlap, some of the solutions found are similar to each other. The results of this procedure are shown in Fig. 7 and listed in Table 2.

We find that "model 0" does not converge into a proper fit to the data, mostly because of the significant difference between the [CII] redshift and that of the Lyman-α line. This forces the model to a high expansion velocity (~500 km s^{-1}) and low dust optical depth. This solution is less favored because the assumed emitting source (the C10 galaxy) is a gas-rich dusty galaxy, and the predicted low optical depth is contrary to the high dust content observed in the source (C10) assumed by the model.

The best fits are produced when using higher systemic redshifts (models 1–3), which are more consistent with the redshift of the Lyman-α line. This is the case for sources C14 and C17 and the protocluster core. In these cases, the solutions are similar, yielding high outflow velocities (~300–400 km s^{-1}) and yet very low HI column densities ($\log(N(\mathrm{HI})) \sim 16$). In these cases, the opacities appear to be moderate ($\tau > 1.5$–3.0) yet more consistent with the dusty nature of the purported emission sources. Based on these results alone, it is hard to disentangle the origin of the LAB, and therefore the models are inconclusive. However, for the starbursting galaxies of the protocluster core to produce the Lyman-α emission would require a complex patchy geometry where some of the UV radiation escapes and illuminates the HI gas in the LAB direction. While this is a plausible scenario, and is supported by the moderate optical depth of this solution (model 3), such a solution is less likely than the scenario where the UV radiation is produced in situ by either the C14 or the C17 galaxy, or both.

5. Summary and conclusions

We presented a census of Lyman-α emission toward the IR-bright protocluster SPT2349-56 at $z = 4.3$ obtained using MUSE observations. Through a blind search of Lyman-α emission toward the protocluster core and northern extension, we found three LAEs at distances of >90 kpc from the protocluster core. The LAEs are bound to the $9 \times 10^{12}\ M_{\odot}$ protocluster core, and all of them are redshifted relative to SPT2349-56. Only one of the ALMA SMGs previously identified in this field is tentatively detected in Lyman-α.

Using a continuum-subtracted narrowband image, we detect extended Lyman-α emission, which we refer to as a LAB, with a size of about 70 kpc across, located ~56 kpc to the east of the protocluster core. The bulk of the LAB emission is also redshifted with respect to the core of the protocluster.

Two of the spatially overlapping SMGs, C14, and C17, are found to also coincide spectrally when comparing their [CII] emission lines with that of the Lyman-α emission from the LAB (Miller et al. 2018; Hill et al. 2020). This observation could be explained by the high star-formation activity seen in the SMG protocluster members. Based on their locations and redshifts, the main candidates potentially producing the ionizing photons and thus the Lyman-α emission are the C14 and C17 SMGs or the protocluster core. In the latter case, the geometry of the dust distribution should allow the Lyman-α photons to get scattered from the core such that the photons find a region to escape to the east. Such scenarios are supported by radiative transfer modeling of the Lyman-α line profile of the LAB.

We do not find an overdensity of LAEs or a source density comparable to what we might have expected from the number of [C II] and submillimeter continuum sources found in this field. We interpret this as a structure that is still heavily dust-obscured and dominated by submm-detected galaxies.

Table 2. Results from the radiative transfer modeling of the LAB line profile.

Model	Source [(†)]	z_{sys}	v_{exp} (km s^{-1})	$\log(N_{HI})$ (cm^{-2})	τ_d	$\log(T)$ (K)	EW(Lyman-α) (Å)	σ(Lyman-α) [(‡)] (km s^{-1})
0	C10	4.2895 ± 0.0019	480^{+9}_{-14}	$19.85^{+0.17}_{-0.11}$	$0.01^{+0.02}_{-0.01}$	$4.2^{+0.4}_{-0.6}$	$5.1^{+1.3}_{-1.2}$	798^{+15}_{-31}
1	C14	4.3057 ± 0.0020	377^{+28}_{-46}	$16.19^{+0.43}_{-0.22}$	$3.7^{+0.9}_{-1.6}$	$3.1^{+0.4}_{-0.2}$	$6.6^{+0.9}_{-0.8}$	328^{+33}_{-22}
2	C17	4.3049 ± 0.0020	375^{+17}_{-31}	$16.15^{+0.43}_{-0.19}$	$2.8^{+1.1}_{-1.3}$	$3.15^{+0.35}_{-0.23}$	$6.6^{+1.0}_{-0.8}$	330^{+30}_{-16}
3	Core	4.3040 ± 0.0020	310^{+36}_{-22}	$16.65^{+0.39}_{-0.50}$	$1.7^{+1.8}_{-1.2}$	$3.1^{+0.3}_{-0.2}$	$6.6^{+1.1}_{-0.9}$	346^{+42}_{-35}

Notes. [(†)]Source assumed to be producing the Lyman-α emission. Its [CII] redshift is assumed to be the systemic redshift of the system for each model. [(‡)]$\sigma = FWHM/2.35$.

Acknowledgements. This paper makes use of the following ALMA data: ADS/JAO.ALMA#2017.1.00273.S; and ADS/JAO.ALMA#2018.1.00058.S. ALMA is a partnership of ESO (representing its member states), NSF (USA), and NINS (Japan), together with NRC (Canada), MOST, and ASIAA (Taiwan), and KASI (Republic of Korea), in cooperation with the Republic of Chile. The Joint ALMA Observatory is operated by ESO, AUI/NRAO, and NAOJ. Y.A. acknowledges partial support from Comité Mixto ESO – Gobierno de Chile. M.A. acknowledges support from FONDECYT grant 1211951, CONICYT + PCI + Instituto Max Planck de Astronomia MPG190030 and CONICYT+PCI+REDES 190194. This work was partially funded by the ANID BASAL project FB210003. T.A. acknowledges support from the Millennium Science Initiative ICN12_009. D.N. acknowledges support from the US NSF under grant 1715206 and Space Telescope Science Institute under grant AR-15043.0001. J.D.V. and S.J. acknowledges support from the US NSF under grants AST-1715213 and AST-1716127. S.J. acknowledge support from the US NSF NRAO under grants SOSPA5-001 and SOSPA7-006, and SOSPA4-007, respectively. J.D.V. acknowledges support from an A.P. Sloan Foundation Fellowship. E.J.J. acknowledges support from FONDECYT Iniciación en investigación 2020 Project 11200263.

References

Aravena, M., Bertoldi, F., Carilli, C., et al. 2010, ApJ, 708, L36
Arrigoni Battaia, F., Chen, C.-C., Fumagalli, M., et al. 2018, A&A, 620, A202
Bacon, R., Piqueras, L., Conseil, S., Richard, J., & Shepherd, M. 2016, MPDAF: MUSE Python Data Analysis Framework, Astrophysics Source Code Library [record ascl:1611.003]
Baugh, C. M., Cole, S., Frenk, C. S., & Lacey, C. G. 1998, ApJ, 498, 504
Cai, Z., Fan, X., Peirani, S., et al. 2016, ApJ, 833, 135
Cai, Z., Fan, X., Yang, Y., et al. 2017, ApJ, 837, 71
Cantalupo, S. 2017, Astrophys. Space Sci. Lib., 430, 195
Capak, P. L., Riechers, D., Scoville, N. Z., et al. 2011, Nature, 470, 233
Carlstrom, J. E., Ade, P. A. R., Aird, K. A., et al. 2011, PASP, 123, 568
Casey, C. M., Cooray, A., Capak, P., et al. 2015, ApJ, 808, L33
Cen, R., & Zheng, Z. 2013, ApJ, 775, 112
Chapman, S. C., Lewis, G. F., Scott, D., et al. 2001, ApJ, 548, L17
Chapman, S. C., Blain, A., Ibata, R., et al. 2009, ApJ, 691, 560
Chapman, S. C., Hill, R., Aravena, M., et al. 2024, ApJ, 961, 120
Chiang, Y.-K., Overzier, R., & Gebhardt, K. 2013, ApJ, 779, 127
Chiang, Y.-K., Overzier, R. A., Gebhardt, K., et al. 2015, ApJ, 808, 37
Claeyssens, A., Richard, J., Blaizot, J., et al. 2022, A&A, 666, A78
Croft, S., Kurk, J., van Breugel, W., et al. 2005, AJ, 130, 867
Daddi, E., Dannerbauer, H., Stern, D., et al. 2009, ApJ, 694, 1517
De Lucia, G., & Blaizot, J. 2007, MNRAS, 375, 2
Drake, A. B., Garel, T., Wisotzki, L., et al. 2017, A&A, 608, A6
Everett, W. B., Zhang, L., Crawford, T. M., et al. 2020, ApJ, 900, 55
Furlanetto, S. R., Schaye, J., Springel, V., & Hernquist, L. 2005, ApJ, 622, 7
Galametz, A., Stern, D., Pentericci, L., et al. 2013, A&A, 559, A2
Geach, J. E., Narayanan, D., Matsuda, Y., et al. 2016, ApJ, 832, 37
Gronke, M., & Dijkstra, M. 2014, MNRAS, 444, 1095
Gronke, M., Bull, P., & Dijkstra, M. 2015, ApJ, 812, 123
Hashimoto, T., Verhamme, A., Ouchi, M., et al. 2015, ApJ, 812, 157
Hennawi, J. F., Prochaska, J. X., Cantalupo, S., & Arrigoni-Battaia, F. 2015, Science, 348, 779
Herenz, E. C., & Wisotzki, L. 2017, A&A, 602, A111
Hezaveh, Y. D., Marrone, D. P., Fassnacht, C. D., et al. 2013, ApJ, 767, 132
Hill, R., Chapman, S., Scott, D., et al. 2020, MNRAS, 495, 3124
Hill, R., Chapman, S., Phadke, K. A., et al. 2022, MNRAS, 512, 4352
Inami, H., Bacon, R., Brinchmann, J., et al. 2017, A&A, 608, A2
Karim, A., Swinbank, A. M., Hodge, J. A., et al. 2013, MNRAS, 432, 2
Kurk, J. D., Röttgering, H. J. A., Pentericci, L., et al. 2000, A&A, 358, L1
Li, Q., Wang, R., Dannerbauer, H., et al. 2021, ApJ, 922, 236
Magliocchetti, M., Popesso, P., Rosario, D., et al. 2013, MNRAS, 433, 127
Matsuda, Y., Yamada, T., Hayashino, T., et al. 2004, AJ, 128, 569
Miley, G., & De Breuck, C. 2008, A&A Rev., 15, 67
Miller, T. B., Hayward, C. C., Chapman, S. C., & Behroozi, P. S. 2015, MNRAS, 452, 878
Miller, T. B., Chapman, S. C., Aravena, M., et al. 2018, Nature, 556, 469
Oteo, I., Ivison, R. J., Dunne, L., et al. 2018, ApJ, 856, 72
Overzier, R. A. 2016, A&A Rev., 24, 14
Pentericci, L., Roettgering, H. J. A., Miley, G. K., Carilli, C. L., & McCarthy, P. 1997, A&A, 326, 580
Pike, S. R., Kay, S. T., Newton, R. D. A., Thomas, P. A., & Jenkins, A. 2014, MNRAS, 445, 1774
Planck Collaboration XIII. 2016, A&A, 594, A13
Reuter, C., Vieira, J. D., Spilker, J. S., et al. 2020, ApJ, 902, 78
Rigby, E. E., Hatch, N. A., Röttgering, H. J. A., et al. 2014, MNRAS, 437, 1882
Rotermund, K. M., Chapman, S. C., Phadke, K. A., et al. 2021, MNRAS, 502, 1797
Salpeter, E. E. 1959, ApJ, 129, 608
Shapley, A. E., Steidel, C. C., Pettini, M., & Adelberger, K. L. 2003, ApJ, 588, 65
Smolčić, V., Novak, M., Delvecchio, I., et al. 2017, A&A, 602, A6
Solimano, M., González-López, J., Aravena, M., et al. 2022, ApJ, 935, 17
Song, M., Finkelstein, S. L., Gebhardt, K., et al. 2014, ApJ, 791, 3
Soto, K. T., Lilly, S. J., Bacon, R., Richard, J., & Conseil, S. 2016, MNRAS, 458, 3210
Spilker, J. S., Marrone, D. P., Aravena, M., et al. 2016, ApJ, 826, 112
Steidel, C. C., Adelberger, K. L., Shapley, A. E., et al. 2000, ApJ, 532, 170
Swinbank, A. M., Vernet, J. D. R., Smail, I., et al. 2015, MNRAS, 449, 1298
Umehata, H., Tamura, Y., Kohno, K., et al. 2015, ApJ, 815, L8
Umehata, H., Fumagalli, M., Smail, I., et al. 2019, Science, 366, 97
Venemans, B. P., Kurk, J. D., Miley, G. K., et al. 2002, ApJ, 569, L11
Venemans, B. P., Röttgering, H. J. A., Overzier, R. A., et al. 2004, A&A, 424, L17
Venemans, B. P., Röttgering, H. J. A., Miley, G. K., et al. 2005, A&A, 431, 793
Venemans, B. P., Röttgering, H. J. A., Miley, G. K., et al. 2007, A&A, 461, 823
Verhamme, A., Schaerer, D., & Maselli, A. 2006, A&A, 460, 397
Verhamme, A., Garel, T., Ventou, E., et al. 2018, MNRAS, 478, L60
Vernet, J., Lehnert, M. D., De Breuck, C., et al. 2017, A&A, 602, L6
Vieira, J. D., Crawford, T. M., Switzer, E. R., et al. 2010, ApJ, 719, 763
Vieira, J. D., Marrone, D. P., Chapman, S. C., et al. 2013, Nature, 495, 344
Vito, F., Brandt, W. N., Lehmer, B. D., et al. 2020, A&A, 642, A149
Wang, G. C. P., Hill, R., Chapman, S. C., et al. 2021, MNRAS, 508, 3754
Webb, T. M. A., Yamada, T., Huang, J. S., et al. 2009, ApJ, 692, 1561
Weilbacher, P. M., Streicher, O., Urrutia, T., et al. 2014, ASP Conf. Ser., 485, 451
Zhang, Y., Zheng, X. Z., Shi, D. D., et al. 2022, MNRAS, 512, 4893

Appendix A: Narrowband image

The following figure shows the full extent of the narrowband image obtained from the MUSE cube discussed in Section 3.2.

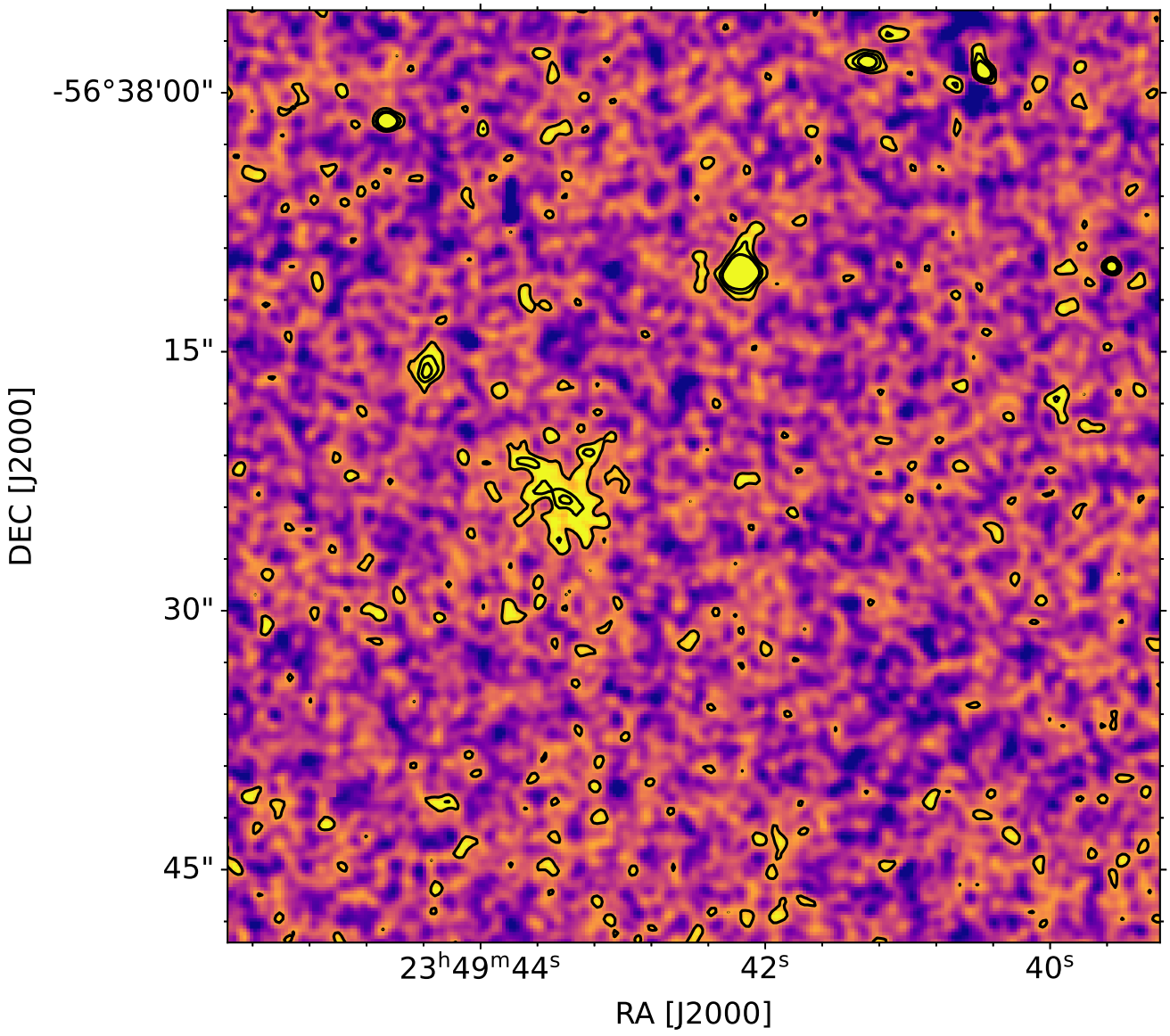

Fig. A.1. Narrowband image of the southern pointing obtained by combining the channels within 1000 km s^{-1} and centered at the protocluster redshift. Black contours show steps at 2, 4, 6, and 8 σ. The location of the LAB can be clearly seen.

Appendix B: Lyman-α spectra toward the SPT2349-56 SMGs

The following figures show the observed MUSE spectra toward all the SMGs in the SPT2349-56 system, centered at the expected location of the Lyman-α line emission.

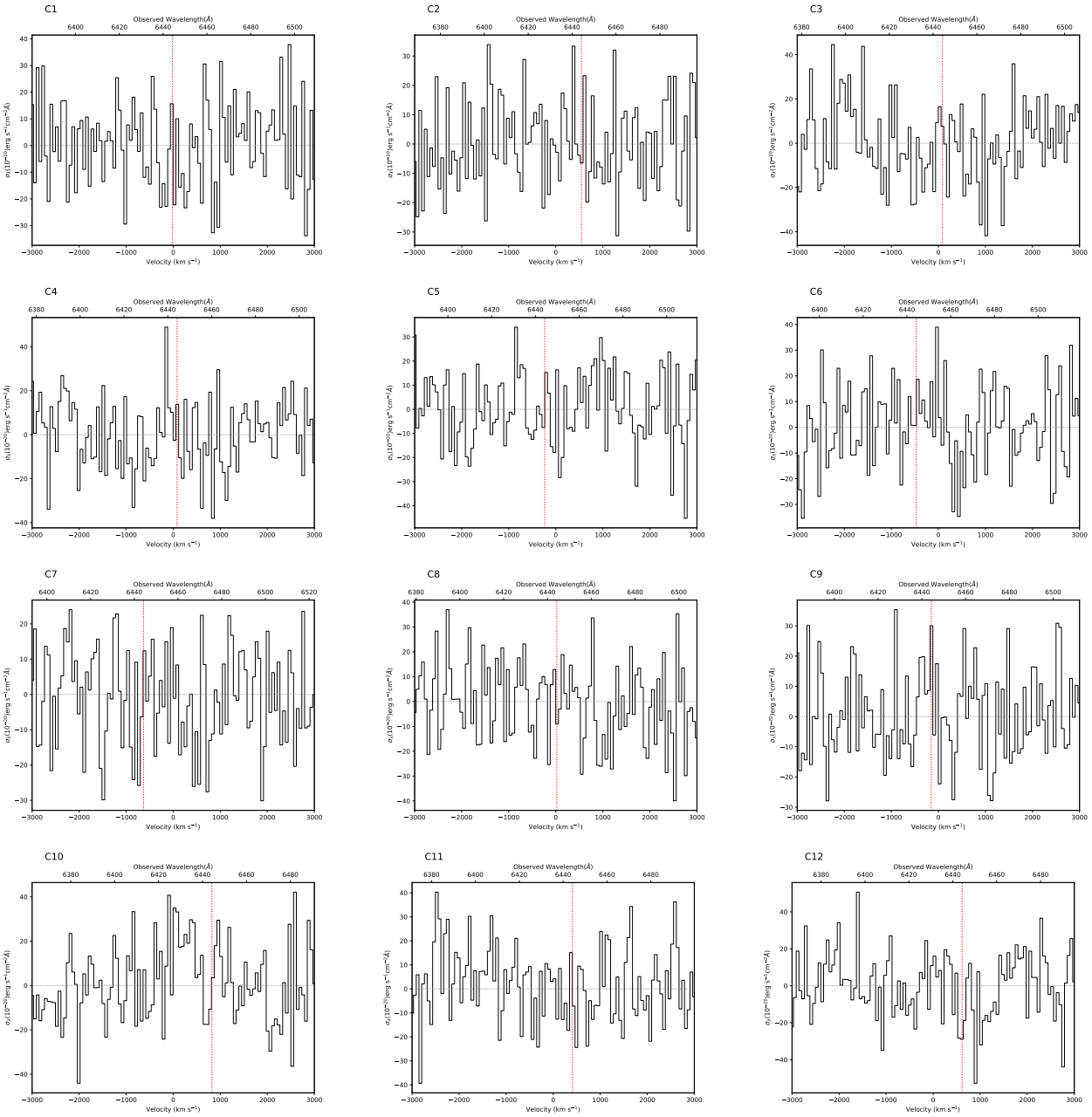

Fig. B.1. MUSE spectra of all the SMGs previously detected toward the SPT2349-56 system at $z = 4.304$. The spectra are centered at the expected wavelength for Lyman-α line emission. The red vertical line highlights the location of the Lyman-α emission line expected from the previous [CII]- or CO-based redshift measurement (Miller et al. 2018; Hill et al. 2020). None of the SMGs are formally detected in Lyman-α emission, and only mild evidence for this line is seen in some of these spectra.

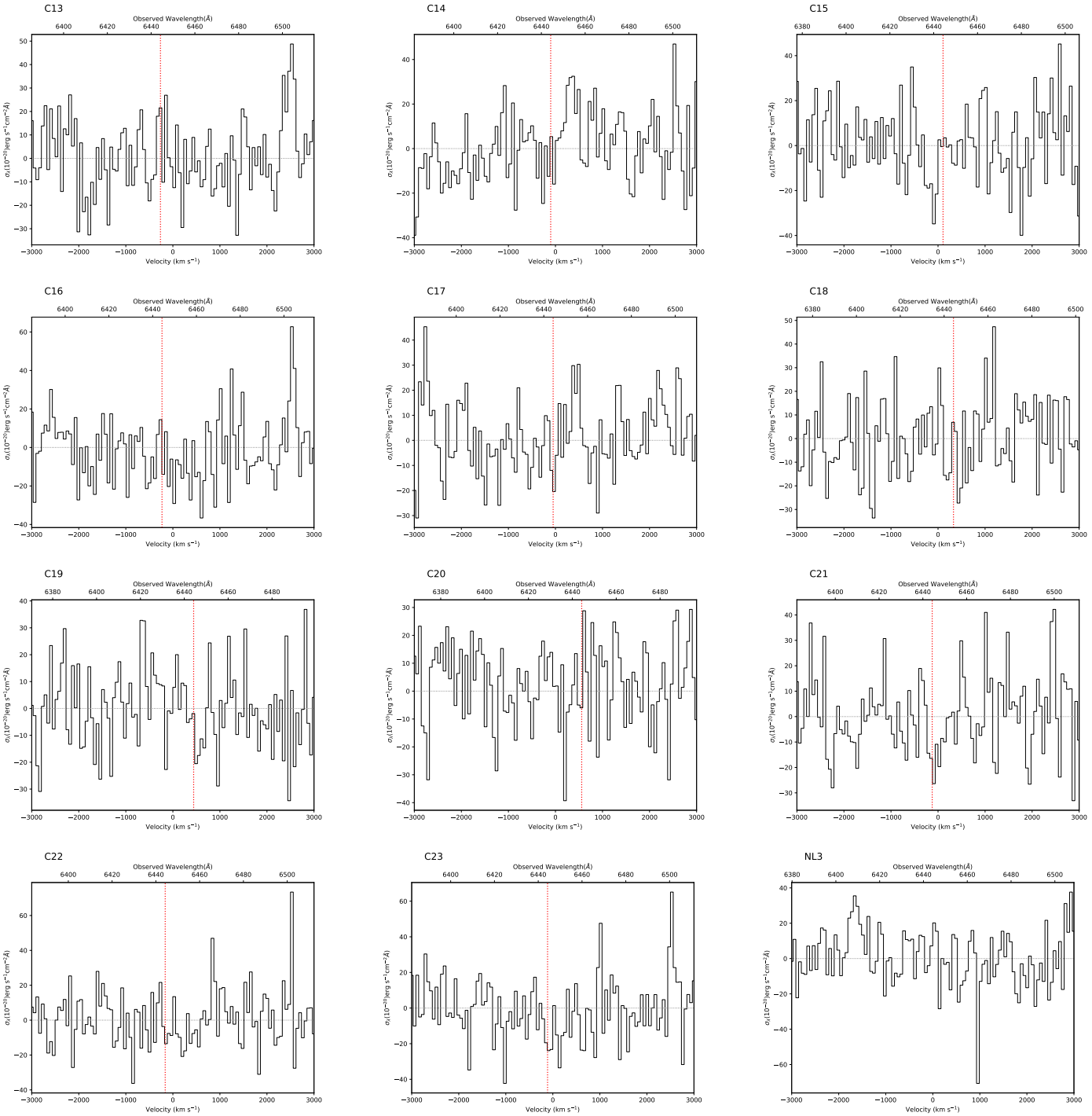

Fig. B.1. Continued.

Appendix C: Detected and confirmed Lyman-α-emitter maps at different wavelengths

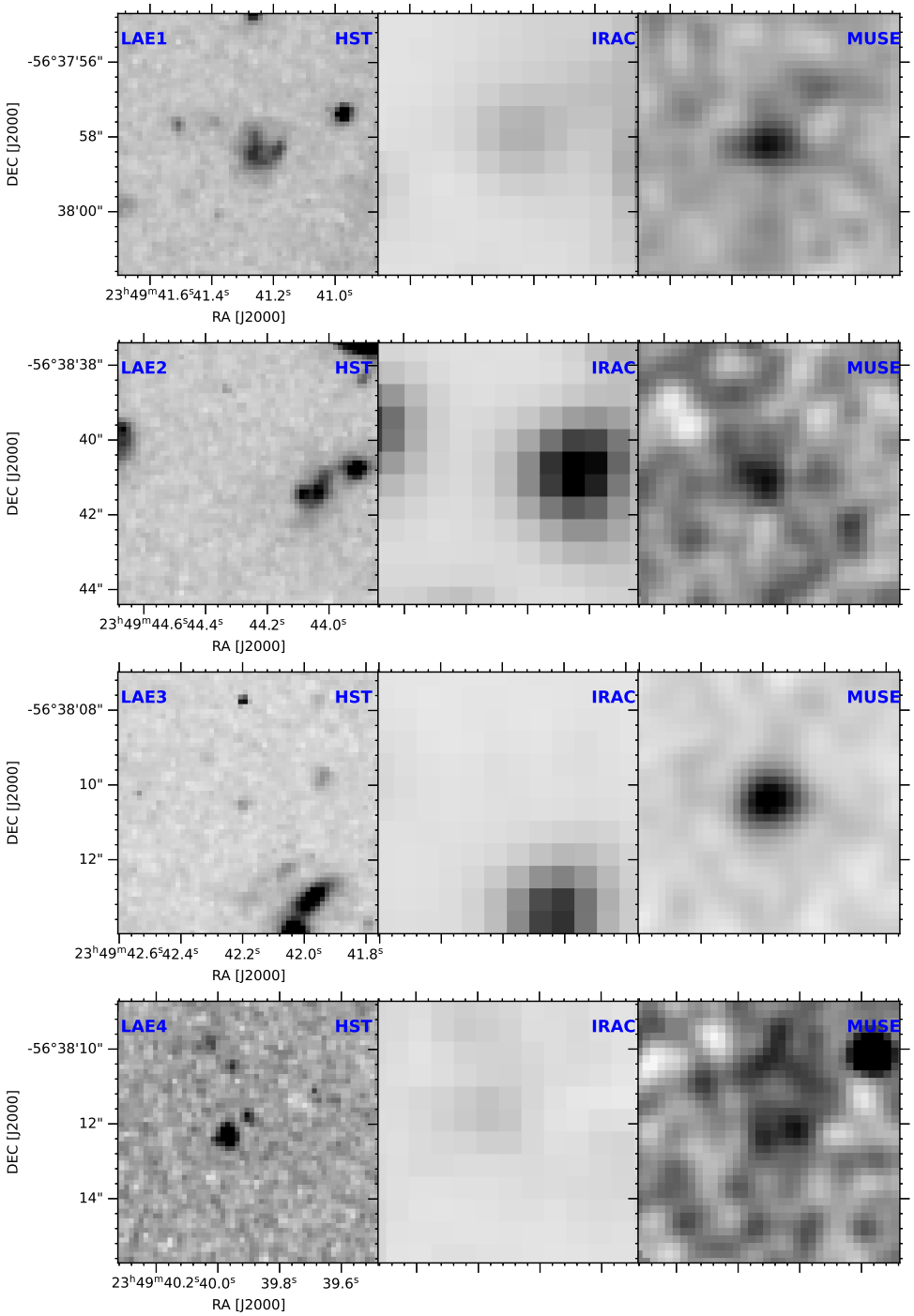

Fig. C.1. Multiwavelength cutouts centered at the position of the LAEs reported in this work. *Left:* HST F160W. *Center:* Ultradeep IRAC mosaic. *Right:* Moment 0 of MUSE.

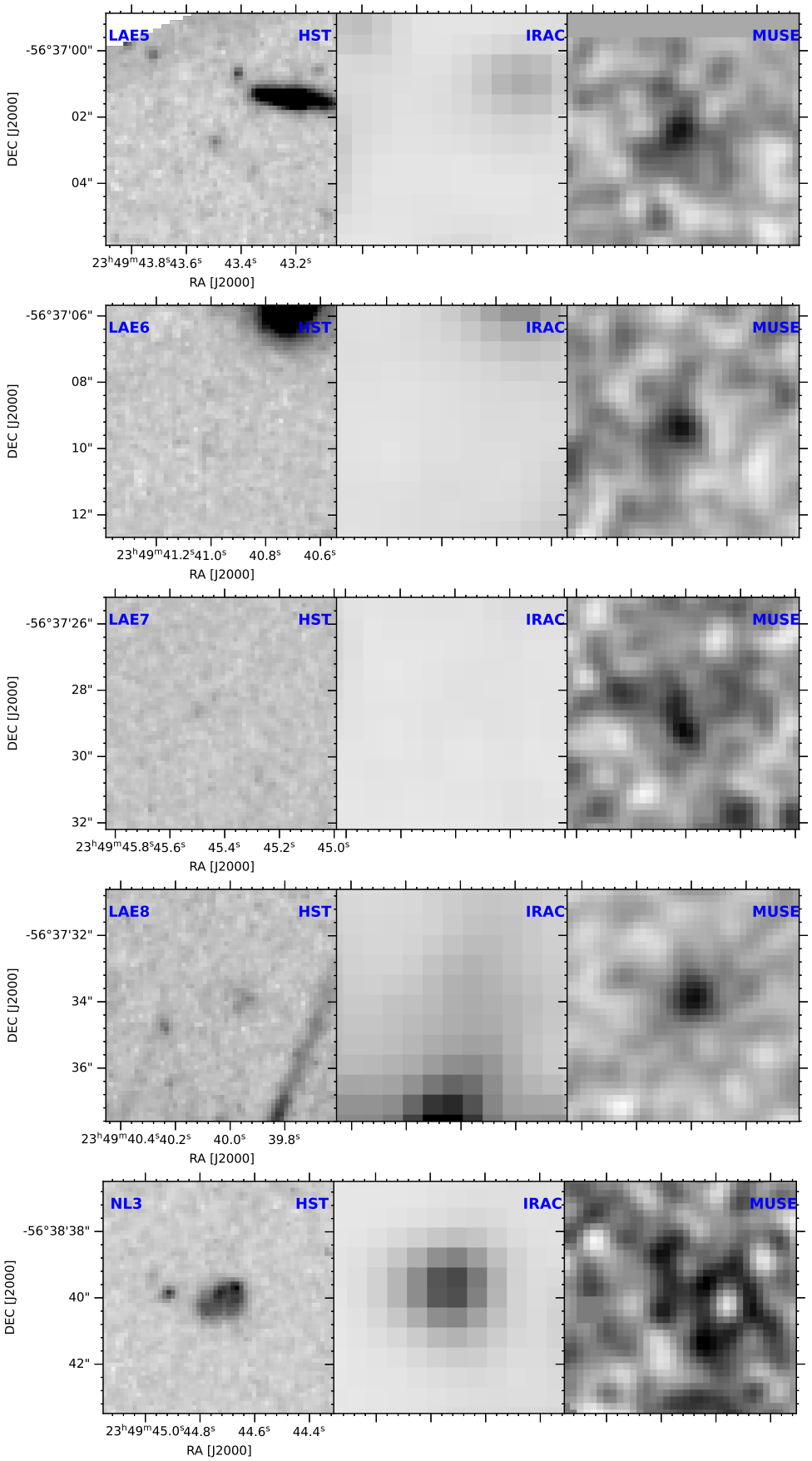

Fig. C.1. Continued.